Editors' Suggestion

SU(4) Chiral Spin Liquid, Exciton Supersolid, and Electric Detection in Moiré Bilayers

Ya-Hui Zhang,[1] D. N. Sheng,[2] and Ashvin Vishwanath[1]
[1]Department of Physics, Harvard University, Cambridge, Massachusetts 02138, USA
[2]Department of Physics and Astronomy, California State University, Northridge, California 91330, USA

(Received 3 May 2021; revised 9 September 2021; accepted 19 November 2021; published 9 December 2021)

We propose a moiré bilayer as a platform where exotic quantum phases can be stabilized and electrically detected. Moiré bilayers consist of two separate moiré superlattice layers coupled through the interlayer Coulomb repulsion. In the small distance limit, an SU(4) spin can be formed by combining layer pseudospin and the real spin. As a concrete example, we study an SU(4) spin model on triangular lattice in the fundamental representation. By tuning a three-site ring exchange term $K \sim (t^3/U^2)$, we find the SU(4) symmetric crystallized phase and an $\mathrm{SU}(4)_1$ chiral spin liquid at the balanced filling. We also predict two different exciton supersolid phases with interlayer coherence at imbalanced filling under displacement field. Especially, the system can simulate an SU(2) Bose-Einstein condensation by injecting interlayer excitons into the magnetically ordered Mott insulator at the layer polarized limit. Smoking gun evidences of these phases can be obtained by measuring the pseudospin transport in the counterflow channel.

DOI: 10.1103/PhysRevLett.127.247701

Introduction.—It is now well appreciated that spin plays an important role in strongly correlated systems. In addition to simple ferromagnetic or antiferromagnetic ordered phases, electronic spins can form nonordered phases such as spin liquids [1–6]. Spin liquids have been found numerically in many spin 1/2 lattice models [7–21], but there is still no well-established evidence in real experiments. One important reason is the difficulty of probing neutral spin excitation. A direct probe of spin transport could provide smoking gun evidence of certain spin liquids, such as the spinon Fermi surface state and chiral spin liquid. Alas, measuring spin transport in traditional solid state systems is unfeasible. Here, we propose to measure the transport of a pseudospin formed by the layer degree of freedom in an electronic material based on two Coulomb coupled moiré superlattices, which we dub as the moiré bilayer.

To build a moiré bilayer, we wish to stack two 2D lattices and forbid their interlayer tunneling. The total charge N_a of each layer $a = 1, 2$ is separately conserved and we can label two quantum numbers as $Q = N_1 + N_2$ and $P_z = \frac{1}{2}(N_1 - N_2)$. P_z can be viewed as a pseudospin. Actually, in the limit that the interlayer distance d is much smaller than the lattice constant a_M, there is a good SU(2) symmetry in the layer pseudospin space, similar to the well studied quantum Hall bilayer [22–24]. Superlattices with $a_M \sim 10$ nm have been recently created in several moiré systems based on graphene [25–37] and transition metal dichalcogenides (TMD) [38–40]. The moiré systems based on graphene generically exhibit ferromagnetic spin coupling due to band topology [29,31–37]. To search for spin liquid, we will use moiré superlattice based on TMD as a building block, where antiferromagnetic spin coupling was demonstrated [38]. We propose two different ways to generate double moiré layers with two triangular moiré superlattices stacked together, as illustrated in Fig. 1.

At integer total filling ν_T, the system is in a Mott insulating phase if U/t is large. There is an SU(4) spin formed by the layer pseudospin $\vec{P}$ and the real spin $\vec{S}$. Just as a concrete illustration, we focus on filling $\nu_T = 1, 3$ and

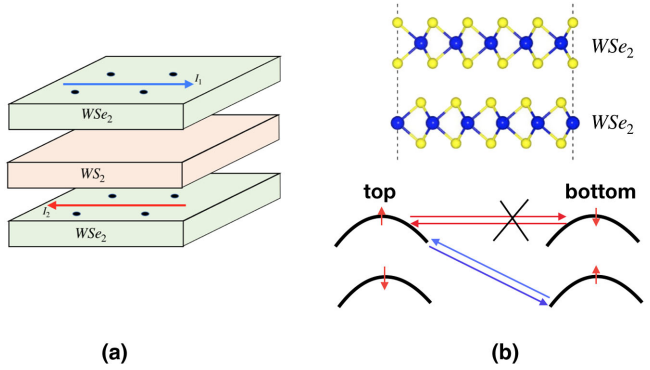

FIG. 1. Two ways of obtaining double moiré superlattice: (a) WSe_2-WS_2-WSe_2 sandwich with both WSe_2 layers aligned with WS_2. A triangular moiré superlattice can be generated for each WSe_2 due to the lattice mismatch between WSe_2 and WS_2 [38,39,41]. WS_2 also acts an insulating barrier to suppress interlayer tunneling between the two WSe_2 layers. (b) Twisted AB stacked TMD homobilayer. The top figure is a side view of the AB stacked bilayer WSe_2 system. The blue and yellow atom label W and Se atoms, respectively. One can see that the W and Se atom of the two layers are aligned vertically. The bottom figure illustrates the spin of the valence bands for the two TMD layers at the same valley, which leads to suppression of interlayer tunneling for the low energy moiré band generated at small twist angle.

map out the phase diagram of an SU(4) spin model generated by t/U expansion up to $O(t^3/U^2)$. We find the large N mean field calculation is in surprisingly good agreement with DMRG simulation, suggesting that mean field calculation is justified for $N \geq 4$. This paves the way to applying mean field calculation to models in more complicated lattices, especially in three dimensions. One interesting phase we found is an $SU(4)_1$ chiral spin liquid stabilized by a three-site ring exchange term. Chiral spin liquids [3,42] have been found to be the ground state for various spin 1/2 lattice models [17–21,43–50] and also in the $SU(N)$ model with $N > 2$ [51–57]. Compared to the early studies, the CSL in our model has a large spin gap (at order of J) and is stabilized in a wide range of t/U. More importantly, in the moiré bilayer setting up, smoking gun evidence of it can be obtained by measuring a quantized Hall effect of the layer pseudospin in counterflow. In moiré bilayer, it is also easy to control the layer polarization P_z continuously. When varying P_z from 0 to fully layer polarized, we also find two different supersolid phases with interlayer coherence (exciton condensation) at small the P_z and large P_z limit, respectively.

Realization of SU(4) Hubbard model.—We first derive an SU(4) Hubbard model for moiré bilayer based on WSe_2-WS_2-WSe_2 or twisted AB stacked WSe_2 homobilayer, as illustrated in Fig. 1. Both systems will host two triangular superlattices in the two WSe_2 layers. In the Supplemental Material [58] we derive the lattice Hubbard model on the triangular lattice by explicitly constructing Wannier orbitals and projecting the Coulomb interaction. One key ingredient is the suppression of the interlayer tunneling due to either insulating barrier (WSe_2-WS_2-WSe_2) or spin conservation (twisted AB stacked WSe_2 bilayer). Our modeling is a straightforward generalization of the previous study of the spin-1/2 Hubbard model in a single moiré layer [41,59], which is now well established by experiments [38,39]. In the end we have four flavors by combining layer pseudospin and the real spin (see the Supplemental Material [58] for more discussions, which includes Ref. [60–64]). The Low energy model is

$$H = -t\sum_{\langle ij\rangle}(c^{\dagger}_{i;a}c_{j;\alpha} + \text{H.c.}) + \frac{U}{2}n_i(n_i - 1), \qquad (1)$$

with $\alpha = a,\ \sigma.\ a = t,\ b$ is the pseudospin index which labels the top and bottom layer. $\sigma = \uparrow, \downarrow$ labels the real spin (locked to the valley) [65]. $c^{\dagger}_{i;a,\sigma}$ creates an electron on moiré site i [66]. There are also small easy-plane anisotropy terms due to finite layer separation. We will ignore them for now.

In this Letter we will focus on the large U/t regime at $\nu_T = 1, 3$, where there is an SU(4) spin in the fundamental representation at each site. At filling $\nu_T = 3$, at the large U/t limit, the spin physics of the Mott insulator is captured by the following $J - K$ model:

$$H = J\sum_{\langle ij\rangle}P_{ij} + 3K\cos\Phi\sum_{\langle ijk\rangle\in\triangle/\triangledown}(P_{ijk} + P_{kji}) + 3K\sin\Phi\sum_{\langle ijk\rangle\in\triangle/\triangledown}(iP_{ijk} - iP_{kji}), \qquad (2)$$

where each bond and each triangle should be counted only once. Φ is the magnetic flux through each triangle. We will focus primarily on the $\Phi = 0$ case with a time reversal symmetry. We have $J = 2(t^2/U) - 12(t^3/U^2)$ and $K = 2(t^3/U^2)$. For $\nu_T = 1$, we just need to replace t with $-t$. In the above P_{ij} and P_{ijk} are two-site and three-site ring-exchange terms. For the triangular lattice, we define the two unit vectors to be $\mathbf{a}_1 = (1, 0)$ and $\mathbf{a}_2 = [-\frac{1}{2}, (\sqrt{3}/2)]$. In the DMRG calculation, we use the boundary condition that $S(\mathbf{r} + L_y\mathbf{a}_2) = S(\mathbf{r})$. The Hilbert space at each site is constructed as a tensor product of two spin 1/2 (layer pseudospin $\vec{P}$ and real spin $\vec{S}$) and we label the corresponding Pauli matrix as τ_μ and σ_μ, respectively. In this representation the generator of the SU(4) can be labeled as $S_{\mu\nu} = \tau_\mu \otimes \sigma_\nu$, $\mu, \nu = 0, x, y, z$.

Phase diagram at balanced filling.—We obtain a phase diagram at $\Phi = 0$ by tuning K/J as shown in Fig. 2 by both DMRG simulation and large N mean field calculation [58]. We find three phases: a crystal with a 2×1 or 2×2 unit cell (spin crystal) [55], a chiral spin liquid (CSL), and a phase with a decoupled 1D chain (DC). The CSL is in the range $K/J \in [0.055, 0.165]$, or, equivalently, $t/U \in [0.041, 0.082]$ or $U/t \in [12.2, 24.4]$. At the upper critical value, higher order spin ring exchange terms may be needed [67], which we leave to future work. A remarkable

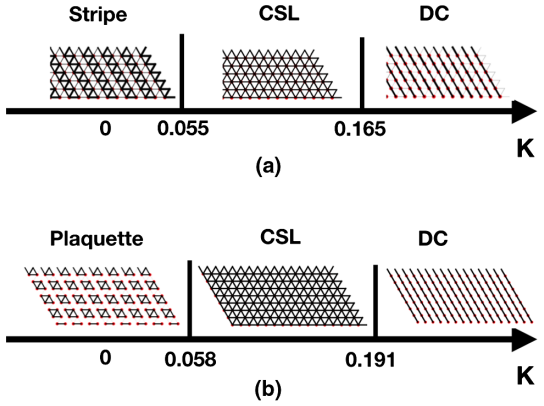

FIG. 2. Phase diagram from (a) DMRG and (b) large-N mean field calculation (Note we have set $J = 1$) at $\Phi = 0$ at balanced filling. (a) Typical patterns of bond order $\langle \tilde{P}_{ij}\rangle$ for the three phases. They are obtained for $K = 0$, $K = 0.114$, and $K = 0.27$ from finite DMRG calculation at $L_y = 6$. In DMRG calculation we find a stripe phase at $K = 0$, but we believe it is unstable to plaquette order in the large L_y limit (see the Supplemental Material [58]). The phase boundaries in DMRG are based on $L_y = 8$ and are already in fairly good agreement with the large-N result.

observation is that the phase diagram obtained in DMRG is in good agreement with that of a simple large N mean field calculation. Note that our result at the Heisenberg limit $K = 0$ does not agree with a previous DMRG study [68] and we do not find signature of resonating plaquette order [69]. For DMRG simulations, we keep the bond dimension to be between 4000 and 10 000 with a truncation error at the order of 10^{-4} for $L_y = 6$ and 8 and smaller for $L_y = 4$, providing accurate results through finite bond dimension analysis (see Fig. 4 in the Supplemental Material [58] for more details).

Let us also provide some intuition why the CSL and the DC phase are stabilized by $K > 0$. The three-site ring exchange term can be written as $\tilde{P}_{ijk} + \text{H.c} = -8[\vec{S}_i \cdot (\vec{S}_j \times \vec{S}_k)][\vec{P}_i \cdot (\vec{P}_j \times \vec{P}_k)] + 2\sum_{\tilde{i}\tilde{j}\tilde{k}} (\vec{S}_{\tilde{i}} \cdot \vec{S}_{\tilde{k}})(\vec{P}_{\tilde{j}} \cdot \vec{P}_{\tilde{k}})$. When $K > 0$, the first term favors onset of chirality order $\langle \vec{S}_i \cdot (\vec{S}_j \times \vec{S}_k) \rangle = \langle \vec{P}_i \cdot (\vec{P}_j \times \vec{P}_k) \rangle \neq 0$, leading to the CSL phase. The second term penalizes coexistence of two dimerized bonds for each triangle, favoring the decoupled chain phase. In contrast, the $K < 0$ side suppresses chirality orders and favors plaquette order.

The $SU(4)_1$ chiral spin liquid.—Next we move to a detailed study of the CSL. First, at $\Phi = 0$, we find long range correlation of chirality order, as shown in Fig. 3(a), suggesting spontaneous breaking of the time reversal symmetry. In Fig. 3(b) we show the chirality order parameter with K/J for $L_y = 4$, 6, 8. We can see that the phase boundaries from $L_y = 6$ and $L_y = 8$ are close. In the Supplemental Material [58] we show that the CSL phase has a spin gap $\Delta_S \sim J$ and a correlation length $\xi_S < 1$, therefore $L_y = 6$, 8 are much larger than the correlation length and may already be in the 2D limit. The $SU(4)_1$ CSL has a chiral edge described by the $SU(4)_1$ chiral CFT. It consists of three chiral boson and its entanglement spectrum should show a degeneracy of 1,3,9,22,… for a given spin sector [52]. Precisely such a sequence is confirmed by our DMRG calculation in Fig. 3(c).

The CSL has a spin Hall conductivity σ_{xy} which can be measured in DMRG via flux insertion [45,70]. For each quantum number $\tilde{Q}_1 = \frac{1}{4}(S_{z0} + S_{0z} + S_{zz})$, $\tilde{Q}_2 = \frac{1}{4}(S_{z0} - S_{0z} - S_{zz})$, $\tilde{Q}_3 = \frac{1}{4}(-S_{z0} + S_{0z} - S_{zz})$, we define a twisted boundary condition $S(\mathbf{r} + Ly\mathbf{a_2}) = U_I^\dagger(\varphi) S(\mathbf{r}) U_I(\varphi)$, where $U_I(\varphi) = e^{i\tilde{Q}_I \varphi}$ and $S(\mathbf{r})$ is an arbitrary spin operator at site $\mathbf{r}$. Note that $U_I(\varphi = 2\pi) = e^{-i(2\pi/4)} I$ is a Z_4 flux insertion. In Fig. 3(d) we show the spin pumping generated by $U_1(\varphi)$, which implies spin Hall conductivity $\tilde{\sigma}_{xy}^{i1} = (\frac{3}{4}, -\frac{1}{4}, -\frac{1}{4})$ for $i = 1, 2, 3$. The pumping of $U_2(\varphi)$ and $U_3(\varphi)$ give consistent results and we get

$$\tilde{\sigma}_{xy} = \frac{1}{4} \begin{pmatrix} +3 & -1 & -1 \\ -1 & +3 & -1 \\ -1 & -1 & +3 \end{pmatrix}$$

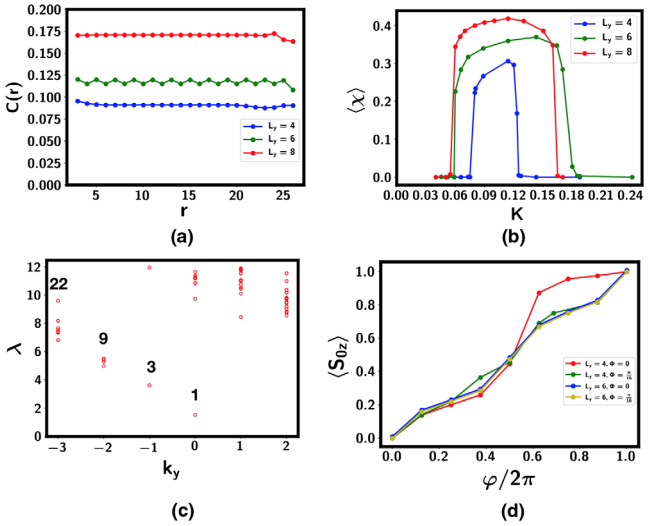

FIG. 3. (a) Correlation function of the chirality order at $K = 0.114$ (we have set $J = 1$ here) using a real code (with real wave function) to enforce the time reversal symmetry. Note that the ground state is forced to be a superposition of one chiral state and its time reversal partner. $C(\mathbf{r}) = \langle \chi(\mathbf{r}) \chi(0) \rangle$, where $\chi = i(P_{ijk} - \text{H.c.})$ is the chirality order parameter. (b) The chirality order $\langle \chi(r) \rangle$ obtained from finite DMRG with complex code, where the ground state is in just one chiral state. The chirality order $\chi_{ijk} = \langle i(P_{ijk} - \text{H.c}) \rangle$ is defined for each triangle. (c) Entanglement spectrum from finite DMRG at $K = 0.114$ and $\Phi = \pi/16$ for $L_y = 6$. Weak explicit time reversal breaking was included to enhance clarity. There is a chiral edge mode with degeneracy 1,3,9,22. (d) Change in $\langle S_{0z} \rangle$ on the left side of the cylinder, pumped by the flux insertion generated by $U_1(\varphi) = e^{i\tilde{Q}_1 \varphi}$. Pumping of S_{z0} and S_{zz} are exactly the same and thus not shown. In the basis $\tilde{Q}_1 = \frac{1}{4}(S_{z0} + S_{0z} + S_{zz})$, $\tilde{Q}_2 = \frac{1}{4}(S_{z0} - S_{0z} - S_{zz})$, $\tilde{Q}_3 = \frac{1}{4}(-S_{z0} + S_{0z} - S_{zz})$, the pumped charges are $\delta\tilde{Q}_1 = \frac{3}{4}$, $\delta\tilde{Q}_2 = \delta\tilde{Q}_3 = -\frac{1}{4}$.

which is nothing but the inverse of the K matrix [58]:

$$K = \begin{pmatrix} 2 & 1 & 1 \\ 1 & 2 & 1 \\ 1 & 1 & 2 \end{pmatrix}$$

[71].

We also studied the effect of SU(4) breaking anisotropy term $H_S = \delta J \sum_{\langle ij \rangle} (P_{i;x} P_{j;x} + P_{i;y} P_{j;y})(4\vec{S}_i \cdot \vec{S}_j + S_{i;0} S_{j;0}) + 2(\delta J + \delta V) \sum_{\langle ij \rangle} P_{i;z} P_{j;z}$ caused by the finite interlayer distance. We find that the CSL phase is stable when $\delta J/J < 0.5$, $\delta V/J < 0.5$ in DMRG calculation [58], which is satisfied when the interlayer distance $d < 1$ nm [58].

Supersolids at imbalanced filling.—In the moiré bilayer setting up, we can also consider imbalanced filling with the density of the two layers to be $n_t = \frac{1}{2} + \frac{1}{2}\delta$ and $n_b = \frac{1}{2} - \frac{1}{2}\delta$. We study the effect of nonzero δ by fixing $P_z = \frac{1}{2}\delta$ in the DMRG calculation (see Fig. 4.) Here we note two supersolid phases found at $K = 0$: (i) *Supersolid on top of stripe*

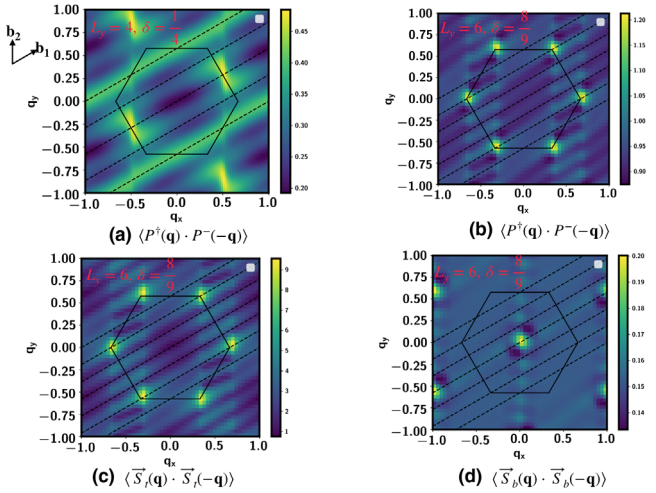

FIG. 4. Spin and exciton structure factor from infinite DMRG at imbalanced filling. q_x, q_y is in the unit of $2\pi/a$, where a is the lattice constant. We parametrize the momentum as $\mathbf{q} = q_1\mathbf{b_1} + q_2\mathbf{b_2}$, where $\mathbf{b_1}$ and $\mathbf{b_2}$ are reciprocal vectors. The solid hexagon is the Brillouin zone and the dashed lines are the well-defined momentum cut along $q_2 = (1/L_y)n$ with n an integer. (a) Exciton order correlation function $P^{\dagger}(\mathbf{q})P^{-}(-\mathbf{q})$ has a peak at the M point with momentum $\frac{1}{2}\mathbf{b_1}$ at small δ. There is also a feature along the $q_2 = \pm\frac{1}{2}$ cut without dispersion along $\mathbf{b_1}$. This is consistent with a decoupled stripe phase at the $\delta = 0$ limit. At δ close to 1: (b) the exciton order parameter is peaked at the K,K' point. (c) The spin $\vec{S}_t$ at the top layer is ordered at momentum K, K', consistent with a 120° order. (d) The spin $\vec{S}_b$ at the bottom layer is ferromagnetically ordered.

phase: When δ is small, DMRG shows a stripe phase with bond pattern similar to the $K = 0$ point at $\delta = 0$ in Fig. 2(a). On top of the stripe phase, we find exciton condensation at momentum M, as indicated by correlation function of exciton order $P^{\dagger} = P_x + iP_y$ shown in Fig. 4(a). The real spin in this phase is not ordered. The exciton condensate has a spatial structure due to its nonzero momentum M and hence can be called a supersolid phase; see Fig. 4(a). (ii) *Spinful BEC at the layer polarized limit:* When $\delta = 1$–$2x$ with small x, we can start from the 120° Neel order in the top layer at the $n_t = 1$, $n_b = 0$ limit and then inject interlayer excitons with density x. The interlayer exciton carries an SU(2) spin index from the bottom layer [72]. Finally, the system simulates a gas of spinful bosons on triangular lattice at total density x. The ground state is known to be a spin-polarized Bose-Einstein condensation (BEC) of the excitons. The real spin in this phase is in the 120° ordered and ferromagnetic ordered phase, respectively, for the two layers, as confirmed by DMRG results shown in Figs. 4(b),4(c),4(d). Two recent experiments studied the transferring of interlayer excitons starting from a layer polarized Mott insulator [73,74]. The low energy physics of the exciton and spin in these systems should be very similar to the model we study here [75]. Therefore our prediction of a spin 1/2 BEC could be directly relevant to these experiments.

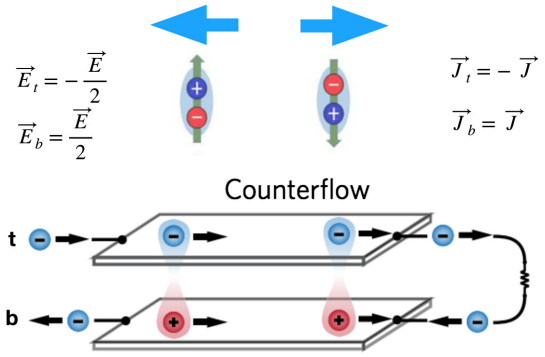

FIG. 5. Counterflow measurement of the transport of the electric dipole moment carried by the interlayer exciton. t, b labels the top and bottom layer, respectively. $\vec{E}_d = \vec{E}_t - \vec{E}_b$ is the dipole electric field and $\vec{J}_d = \frac{1}{2}(\vec{J}_t - \vec{J}_b)$ is the dipole current. Under $\vec{E}_d$, the dipole moment feels a force $\vec{F}_d = P_z\vec{E}_d$. In the $SU(4)_1$ CSL, there is a dipole quantum Hall effect: $\sigma^d_{xy} = (J^x_d/E^y_d) = \pm(e^2/h)$. For the supersolid phase with interlayer coherence, the counterflow behavior is the same as a superfluid phase.

Experimental detection.—Here we point out that it is possible to obtain smoking gun evidences for the CSL phase and the supersolid phase in moiré bilayer in counterflow transport, as shown in Fig. 5. The counterflow measures the current of the layer pseudospin P_z, which carries an electric dipole moment. A dipole quantum Hall effect with $\sigma^d_{xy} = \pm(e^2/h)$ (see Fig. 5) is a direct evidence of the chiral spin liquid. For a supersolid phase with interlayer coherence, we expect a typical superfluid behavior with zero counterflow resistivity. Counterflow has already been implemented in the quantum Hall bilayer to probe different physics [22,24,76], thus the measurement is likely feasible also in the moiré bilayer following our proposal, offering a new application of the counterflow to probe the spin physics of a Mott insulator.

Summary.—In conclusion, we proposed moiré bilayer as a new Hubbard model simulator, where the layer degree of freedom can simulate a pseudospin. This enables electric measurement of the pseudospin transport. We focus on filling $\nu_T = 1, 3$ in the strong Mott limit, and find plaquette order, chiral spin liquid, and the supersolid phase. In the counterflow transport, they will behave as a trivial insulator, quantum Hall insulator, and superfluid. The high controllability of the moiré systems potentially allows for the phase diagram obtained here to be explored by tuning the filling imbalance δ and U/t. We believe the moiré bilayer is promising to shed light on strongly correlated problems with spin playing an essential role. The ability of measuring spin and charge transport separately also makes it possible to test spin-charge separation in the potential exotic metallic state upon slightly doping the Mott inuslator.

Y. H. Z. thanks T. Senthil for discussion and support for DMRG study at early stage of this work. A. V. and Y. H. Z. thank Cory Dean, Philip Kim, and Yihang Zeng for useful discussions. A. V. and Y. H. Z. acknowledge support from a 2019 grant from the Harvard Quantum Initiative Seed Funding program, a Simons Investigator Fellowship, and the Simons Collaboration on Ultra-Quantum Matter, which is a grant from the Simons Foundation (651440, A. V.). D. N. S. was supported by the U.S. Department of Energy, Office of Basic Energy Sciences under Grant No. DE-FG02-06ER46305. The iDMRG simulation was performed using the TeNPy Library (version 0.4.0) [77].

[1] P. W. Anderson, Mater. Res. Bull. **8**, 153 (1973).
[2] P. W. Anderson, Science **235**, 1196 (1987).
[3] V. Kalmeyer and R. B. Laughlin, Phys. Rev. Lett. **59**, 2095 (1987).
[4] L. Balents, Nature (London) **464**, 199 (2010).
[5] L. Savary and L. Balents, Rep. Prog. Phys. **80**, 016502 (2017).
[6] J. Knolle and R. Moessner, Annu. Rev. Condens. Matter Phys. **10**, 451 (2019).
[7] S. Yan, D. A. Huse, and S. R. White, Science **332**, 1173 (2011).
[8] S. Depenbrock, I. P. McCulloch, and U. Schollwöck, Phys. Rev. Lett. **109**, 067201 (2012).
[9] H.-C. Jiang, Z. Wang, and L. Balents, Nat. Phys. **8**, 902 (2012).
[10] L. Wang, D. Poilblanc, Z.-C. Gu, X.-G. Wen, and F. Verstraete, Phys. Rev. Lett. **111**, 037202 (2013).
[11] Y. Iqbal, F. Becca, S. Sorella, and D. Poilblanc, Phys. Rev. B **87**, 060405(R) (2013).
[12] S.-S. Gong, W. Zhu, L. Balents, and D. N. Sheng, Phys. Rev. B **91**, 075112 (2015).
[13] Y.-C. He, M. P. Zaletel, M. Oshikawa, and F. Pollmann, Phys. Rev. X **7**, 031020 (2017).
[14] Z. Zhu, P. A. Maksimov, S. R. White, and A. L. Chernyshev, Phys. Rev. Lett. **120**, 207203 (2018).
[15] S. Hu, W. Zhu, S. Eggert, and Y.-C. He, Phys. Rev. Lett. **123**, 207203 (2019).
[16] S.-S. Gong, W. Zheng, M. Lee, Y.-M. Lu, and D. N. Sheng, Phys. Rev. B **100**, 241111(R) (2019).
[17] C. Hickey, L. Cincio, Z. Papić, and A. Paramekanti, Phys. Rev. B **96**, 115115 (2017).
[18] Z. Zhu, D. N. Sheng, and A. Vishwanath, arXiv: 2007.11963.
[19] A. Szasz and J. Motruk, Phys. Rev. B **103**, 235132 (2021).
[20] A. Wietek, R. Rossi, F. Šimkovic IV, M. Klett, P. Hansmann, M. Ferrero, E. M. Stoudenmire, T. Schafer, and A. Georges, Phys. Rev. X **11**, 041013 (2021).
[21] B.-B. Chen, Z. Chen, S.-S. Gong, D. N. Sheng, W. Li, and A. Weichselbaum, arXiv:2102.05560.
[22] J. Eisenstein, Annu. Rev. Condens. Matter Phys. **5**, 159 (2014).
[23] J. Li, T. Taniguchi, K. Watanabe, J. Hone, and C. Dean, Nat. Phys. **13**, 751 (2017).
[24] X. Liu, K. Watanabe, T. Taniguchi, B. I. Halperin, and P. Kim, Nat. Phys. **13**, 746 (2017).
[25] Y. Cao, V. Fatemi, A. Demir, S. Fang, S. L. Tomarken, J. Y. Luo, J. D. Sanchez-Yamagishi, K. Watanabe, T. Taniguchi, E. Kaxiras *et al.*, Nature (London) **556**, 80 (2018).
[26] G. Chen, A. L. Sharpe, P. Gallagher, I. T. Rosen, E. Fox, L. Jiang, B. Lyu, H. Li, K. Watanabe, T. Taniguchi *et al.*, Nature (London) **572**, 215 (2019).
[27] G. Chen, L. Jiang, S. Wu, B. Lyu, H. Li, B. L. Chittari, K. Watanabe, T. Taniguchi, Z. Shi, J. Jung *et al.*, Nat. Phys. **15**, 237 (2019).
[28] M. Yankowitz, S. Chen, H. Polshyn, Y. Zhang, K. Watanabe, T. Taniguchi, D. Graf, A. F. Young, and C. R. Dean, Science **363**, 1059 (2019).
[29] G. Chen, A. L. Sharpe, E. J. Fox, Y.-H. Zhang, S. Wang, L. Jiang, B. Lyu, H. Li, K. Watanabe, T. Taniguchi *et al.*, Nature (London) **579**, 56 (2020).
[30] X. Lu, P. Stepanov, W. Yang, M. Xie, M. A. Aamir, I. Das, C. Urgell, K. Watanabe, T. Taniguchi, G. Zhang *et al.*, Nature (London) **574**, 653 (2019).
[31] Y. Cao, D. Rodan-Legrain, O. Rubies-Bigorda, J. M. Park, K. Watanabe, T. Taniguchi, and P. Jarillo-Herrero, Nature (London) **583**, 215 (2020).
[32] X. Liu, Z. Hao, E. Khalaf, J. Y. Lee, Y. Ronen, H. Yoo, D. H. Najafabadi, K. Watanabe, T. Taniguchi, A. Vishwanath *et al.*, Nature (London) **583**, 221 (2020).
[33] C. Shen, Y. Chu, Q. Wu, N. Li, S. Wang, Y. Zhao, J. Tang, J. Liu, J. Tian, K. Watanabe *et al.*, Nat. Phys. **16**, 520 (2020).
[34] H. Polshyn, J. Zhu, M. A. Kumar, Y. Zhang, F. Yang, C. L. Tschirhart, M. Serlin, K. Watanabe, T. Taniguchi, A. H. MacDonald *et al.*, Nature (London) **588**, 66 (2020).
[35] S. Chen, M. He, Y.-H. Zhang, V. Hsieh, Z. Fei, K. Watanabe, T. Taniguchi, D. H. Cobden, X. Xu, C. R. Dean *et al.*, Nat. Phys. **17**, 374 (2021).
[36] A. L. Sharpe, E. J. Fox, A. W. Barnard, J. Finney, K. Watanabe, T. Taniguchi, M. Kastner, and D. Goldhaber-Gordon, Science **365**, 605 (2019).
[37] M. Serlin, C. Tschirhart, H. Polshyn, Y. Zhang, J. Zhu, K. Watanabe, T. Taniguchi, L. Balents, and A. Young, Science **367**, 900 (2020).
[38] Y. Tang, L. Li, T. Li, Y. Xu, S. Liu, K. Barmak, K. Watanabe, T. Taniguchi, A. H. MacDonald, J. Shan *et al.*, Nature (London) **579**, 353 (2020).
[39] E. C. Regan, D. Wang, C. Jin, M. I. B. Utama, B. Gao, X. Wei, S. Zhao, W. Zhao, Z. Zhang, K. Yumigeta *et al.*, Nature (London) **579**, 359 (2020).
[40] L. Wang, E.-M. Shih, A. Ghiotto, L. Xian, D. A. Rhodes, C. Tan, M. Claassen, D. M. Kennes, Y. Bai, B. Kim *et al.*, Nat. Mater. **19**, 861 (2020).
[41] F. Wu, T. Lovorn, E. Tutuc, and A. H. MacDonald, Phys. Rev. Lett. **121**, 026402 (2018).
[42] X.-G. Wen, F. Wilczek, and A. Zee, Phys. Rev. B **39**, 11413 (1989).
[43] B. Bauer, L. Cincio, B. P. Keller, M. Dolfi, G. Vidal, S. Trebst, and A. W. W. Ludwig, Nat. Commun. **5**, 5137 (2014).
[44] Y.-C. He, D. N. Sheng, and Y. Chen, Phys. Rev. Lett. **112**, 137202 (2014).
[45] S.-S. Gong, W. Zhu, and D. N. Sheng, Sci. Rep. **4**, 6317 (2014).
[46] Y.-C. He and Y. Chen, Phys. Rev. Lett. **114**, 037201 (2015).

[47] A. Szasz, J. Motruk, M. P. Zaletel, and J. E. Moore, Phys. Rev. X **10**, 021042 (2020).

[48] W.-J. Hu, S.-S. Gong, and D. N. Sheng, Phys. Rev. B **94**, 075131 (2016).

[49] A. Wietek, A. Sterdyniak, and A. M. Läuchli, Phys. Rev. B **92**, 125122 (2015).

[50] N. Y. Yao, M. P. Zaletel, D. M. Stamper-Kurn, and A. Vishwanath, Nat. Phys. **14**, 405 (2018).

[51] M. Hermele, V. Gurarie, and A. M. Rey, Phys. Rev. Lett. **103**, 135301 (2009).

[52] P. Nataf, M. Lajkó, A. Wietek, K. Penc, F. Mila, and A. M. Läuchli, Phys. Rev. Lett. **117**, 167202 (2016).

[53] J.-Y. Chen, S. Capponi, A. Wietek, M. Mambrini, N. Schuch, and D. Poilblanc, Phys. Rev. Lett. **125**, 017201 (2020).

[54] C. Boos, C. J. Ganahl, M. Lajkó, P. Nataf, A. M. Läuchli, K. Penc, K. P. Schmidt, and F. Mila, Phys. Rev. Research **2**, 023098 (2020).

[55] X.-P. Yao, Y. Gao, and G. Chen, Phys. Rev. Research **3**, 023138 (2021).

[56] Y.-H. Wu and H.-H. Tu, Phys. Rev. B **94**, 201113(R) (2016).

[57] H.-H. Tu, A. E. Nielsen, and G. Sierra, Nucl. Phys. **B886**, 328 (2014).

[58] See Supplemental Material at http://link.aps.org/supplemental/10.1103/PhysRevLett.127.247701 for details on DMRG simulation and modeling of the materials.

[59] F. Wu, T. Lovorn, E. Tutuc, I. Martin, and A. H. MacDonald, Phys. Rev. Lett. **122**, 086402 (2019).

[60] H. Tang, S. Carr, and E. Kaxiras, Phys. Rev. B **104**, 155415 (2021).

[61] Y.-H. Zhang and T. Senthil, Phys. Rev. B **99**, 205150 (2019).

[62] J. Brinckmann and P. A. Lee, Phys. Rev. B **65**, 014502 (2001).

[63] Y.-H. Zhang and A. Vishwanath, arXiv:2005.12925.

[64] H. Georgi, *Lie Algebras in Particle Physics. From Isospin to Unified Theories* (Addison-Wesley, Boston, 1982), Vol. 54.

[65] In TMD, the spin and valley are locked together due to a spin-orbit-coupling (SOC). We can view them together as a standard spin $1/2$ at zero magnetic field, but the g factor is anisotropic due to the SOC. Especially, the Zeeman coupling to the out of plane magnetic field is large and the coupling to in-plane magnetic field is negligible.

[66] Strictly speaking we are doping holes to the valence band of the TMD. But we will still call it electron to match the conventional language.

[67] H.-Y. Yang, A. F. Albuquerque, S. Capponi, A. M. Läuchli, and K. P. Schmidt, New J. Phys. **14**, 115027 (2012).

[68] A. Keselman, B. Bauer, C. Xu, and C.-M. Jian, Phys. Rev. Lett. **125**, 117202 (2020).

[69] K. Penc, M. Mambrini, P. Fazekas, and F. Mila, Phys. Rev. B **68**, 012408 (2003).

[70] R. B. Laughlin, Phys. Rev. B **23**, 5632 (1981).

[71] Note $\tilde{\sigma}_{xy} = K^{-1}$ holds only for the special basis of quantum numbers. For the simplest basis with $Q_1 = S_{z0}$, $Q_2 = S_{0z}$, $Q_3 = S_{zz}$, we have $\sigma_{xy;ab} = 2\delta_{ab}$, with a, $b = 1, 2, 3$. But the flux insertion generated by these simple quantum charges Q_1, Q_2, Q_3 is only Z_2, not the more fundamental Z_4 flux. To generate the Z_4 flux insertion, we need to use a complicated basis $\tilde{Q}_I$, which also lead to $\tilde{\sigma}_{xy} = K^{-1}$.

[72] If we start from the phase with top layer polarized and in a 120° Neel order phase, the interlayer exciton can be labeled as $\Phi_{i;\sigma} = c^{\dagger}_{i;b\sigma} c_{i;t}$, where the spin of $c_{i;t}$ is assumed to be along the 120° order direction at site i. As a result, only the spin of the bottom layer enters the exciton. Note that our system has $\mathrm{SU}(2)_t \times \mathrm{SU}(2)_b$ spin rotation symmetry and $\mathrm{SU}(2)_t$ is already broken by the 120° order.

[73] J. Gu, L. Ma, S. Liu, K. Watanabe, T. Taniguchi, J. C. Hone, J. Shan, and K. F. Mak, arXiv:2108.06588.

[74] Z. Zhang, E. C. Regan, D. Wang, W. Zhao, S. Wang, M. Sayyad, K. Yumigeta, K. Watanabe, T. Taniguchi, S. Tongay *et al.*, arXiv:2108.07131.

[75] Y.-H. Zhang and A. Vishwanath (to be published).

[76] X. Liu, Z. Hao, K. Watanabe, T. Taniguchi, B. I. Halperin, and P. Kim, Nat. Phys. **15**, 893 (2018).

[77] J. Hauschild and F. Pollmann, SciPost Phys. Lect. Notes 5 (2018), https://scipost.org/SciPostPhysLectNotes.5.